Running Title: Mto1 and Mto2 regulate the cleavage furrow

Astral Microtubules Regulate Formation of the Cytokinetic Cleavage Furrow in Fission Yeast

Samantha E. R. Dundon[1] and Thomas D. Pollard[1,2,3,*]

[1]Departments of Molecular Cellular and Developmental Biology
[2]Departments of Molecular Biophysics and Biochemistry
[3]Department of Cell Biology
Yale University, PO Box 208103
New Haven, CT 06520-8103 USA
*Correspondence: thomas.pollard@yale.edu

Summary

Dundon and Pollard show that compromising the Mto1 or Mto2 regulators of the fission yeast γ-tubulin complex reduces or eliminates astral microtubules, exaggerates the effects of a non-lethal D277N substitution in β-glucan synthase 1 (Cps1/Bgs1) on the rate of cytokinetic furrow formation, and increases Rho-GTP at the cleavage site.

Abstract

Microtubules of the mitotic spindle direct cytokinesis in metazoans but this has not been documented in fungi. We report evidence that astral microtubules help coordinate cytokinetic furrow formation in fission yeast. The temperature-sensitive *cps1-191* strain (Liu et al., 1999) with a D277N substitution in β-glucan synthase 1 (Cps1/Bgs1) was reported to arrest with an unconstricted contractile ring. We discovered that rings in *cps1-191* cells do constrict slowly and that an S338N mutation in the *mto2* gene is required with the $bgs1^{D277N}$ mutation to reproduce the *cps1-191* phenotype. Complexes of Mto2 and Mto1 with γ-tubulin regulate microtubule assembly. Deletion of Mto1 along with the $bgs1^{D277N}$ mutation also gives the *cps1-191* phenotype, which is not observed in $mto2^{S338N}$ or *mto1Δ* cells expressing $bgs1^{+}$. Both $mto2^{S338N}$

and *mto1Δ* cells nucleate fewer astral microtubules than normal and have higher levels of Rho1-GTP at the division site than wild-type cells. We report multiple conditions that sensitize *mto1Δ* and *mto2*^{S338N} cells to furrow ingression phenotypes. (159 words)

Introduction

Animals, fungi, and amoebas use an actomyosin contractile ring to divide. This ring is constructed at the end of the cell cycle in uninucleate cells, and cellular division must only proceed after successful DNA segregation to generate viable daughters. However, the mechanisms communicating DNA status to the contractile ring are still incompletely understood. Failure to correctly orchestrate this process can cause chromosome segregation errors and aneuploidy, which can promote chromosomal instability.

The fission yeast *Schizosaccharomyces pombe* is an excellent model for understanding mitosis and cytokinesis, including the most comprehensive cytokinetic parts list. The timing of mitotic and cytokinetic milestones is highly reproducible and well characterized; the stereotypical size and shape of *S. pombe* cells facilitates rigorous quantitative microscopy; and numerous temperature-sensitive alleles and facile genetic methods enable dissection of molecular processes.

S. pombe cells assemble a contractile ring from precursors called nodes over 10-15 min following separation of the spindle pole bodies (SPBs) at the onset of anaphase at 23°C (Vavylonis et al., 2008). During anaphase B, the ring matures by adding proteins such as the myosin-II isoform, Myp2 (Wu et al., 2003), the major motor for constriction (Laplante et al., 2015). The maturation period ends with onset of constriction 35 min after SPB separation, even if mutations slow the assembly of the ring (Tebbs and Pollard, 2013; Coffman et al., 2009; Roberts-Galbraith et al., 2010; Wang et al., 2014; Laplante et al., 2015). If a ring takes longer than 35 min to assemble, it constricts immediately (Chen and Pollard, 2011; Tebbs and Pollard, 2013; Li et al., 2016).

Three conditions appear to be required to begin furrow ingression: an intact contractile ring; a signal originating from the cell cycle clock; and initiation of septum synthesis. The enzyme β-glucan synthase 1 (Bgs1) is recruited with its regulator Rho1 to the equator where it synthesizes the primary septum (Arellano et al., 1996) and helps anchor the ring to generate inwardly directed force (Arasada and Pollard, 2014; Davidson et al., 2015). Furrow ingression

initially depends on both tension produced by the contractile ring and septum deposition by Bgs1 (Zhou et al., 2015; Thiyagarajan et al., 2015), but after ~50% ingression, septum synthesis alone suffices to complete division (Proctor et al., 2012). Although the septum can be completed in the absence of the actomyosin ring, tension in the ring promotes septum deposition and maintains the circularity of the pore during septum deposition (Zhou et al., 2015; Thiyagarajan et al., 2015). Mutations compromising the contractility or tension in the ring decrease the constriction rate (Pelham and Chang, 2002; Proctor et al., 2012; Laplante et al., 2015; Tebbs and Pollard, 2013; Li et al., 2016). Ring constriction is faster if the internal pressure against which the furrow ingresses is reduced through mutation or increasing the osmolarity of the growth medium (Morris et al., 2019; Proctor et al., 2012). Bgs1, activated by Rho1, synthesizes the primary septum (Cortés et al., 2007). This is followed by synthesis of the secondary septum by Bgs4 (Rho1) and Ags1 (Rho2) (Cortés et al., 2012; 2005; Arellano et al., 1996; Calonge et al., 2000). While Rho activity is required for cytokinesis, it must decrease after septation to allow cell separation (Nakano et al., 1997).

The fascinating fission yeast strain *cps1-191* (Liu et al., 1999) attracted our attention because it seemed to lack some aspect of the signal for initiating ring constriction. Liu et al. created this strain by chemical mutagenesis and reported that the cells arrested at 36°C with two nuclei and an unconstricted cytokinetic ring. They concluded that colonies did not grow at 36°C due to failed cytokinesis. They identified a candidate gene by genetic mapping, complemented temperature sensitivity of the strain with the wild type $cps1^{+}/bgs1^{+}$ gene, identified the D277N substitution in the gene and named the strain *cps1-191* (Liu et al., 1999). Time-lapse microscopy of the *cps1-191* strain confirmed that the nuclei separate normally but actomyosin rings remain intact without constricting for an hour after assembly at the restrictive temperature (Arasada and Pollard, 2014). The *cps1-191* strain has been used in many studies to generate cells with non-constricting actomyosin rings (Pardo and Nurse, 2003; Yamashita et al., 2005; Venkatram et al., 2005; Wachtler et al., 2006; Loo and Balasubramanian, 2008; Roberts-Galbraith et al., 2009) and others.

Based on these reports, we selected the *cps1-191* strain to investigate the mechanisms that initiate cytokinetic ring constriction. However, we determine that rings in *cps1-191* cells do not arrest *per se*, but constrict very slowly and that cells with the $bgs1^{D227N}$ mutation die from lysis at 36°C rather than arresting the cell cycle as previously thought. Surprisingly, we found

that the *cps1-191* constriction phenotype depends on a second point mutation in the gene for the γ-tubulin regulator Mto2, implicating microtubules in the process that drives furrow ingression.

S. pombe has multiple microtubule organizing centers (MTOCs) containing γ-tubulin in addition to the SPB (Sawin and Tran, 2006). During interphase, multiple MTOCs localize along microtubule bundles (Janson et al., 2005). During mitosis, interphase microtubules disassemble and the SPBs nucleate spindle and astral microtubules. Finally, during cytokinesis Myp2 recruits MTOCs to the equator (Samejima et al., 2010), where they nucleate the post-anaphase array (PAA) of microtubules. Mto1 and, to a lesser extent, Mto2 are critical proteins for the function and cell-cycle regulated activities of these MTOCs. In the absence of Mto1, no MTOCs form beyond the SPB, which only nucleates microtubules from its inner face (Zimmerman and Chang, 2005). In biochemical reconstitution experiments, the Mto1/Mto2 complex and MOZART1 homolog Mzt1 are required for γ-tubulin to promote microtubule nucleation (Leong et al., 2019). We find that Mto1/Mto2 complex mutants nucleate fewer than normal numbers of astral microtubules, and report one consequence, higher than normal Rho1-GTP activity at the cleavage site. Our findings reveal a new link between microtubules and furrow ingression in fission yeast.

Results

Cytokinetic furrows ingress slower in the cps1-191 *strain than in cells with the* bgs1^{D277N} *mutation.*

Long time-lapse movies of the *cps1-191* strain with genome-encoded Rlc1-tdTomato (regulatory light chain for both isoforms of myosin-II, Myo2 and Myp2) revealed that the actomyosin ring constricted ~30-fold slower (median 0.02 µm/min) at the restrictive temperature of 36°C than in wild-type cells (median 0.62 µm/min) (Fig. 1A, B). We never observed abnormal ring structures such as detachment from the cell wall (Arasada and Pollard, 2014; Laplante et al., 2015; Cheffings et al., 2019), therefore we consider Rlc1-tdTomato constriction to reflect furrow ingression. Thirty percent of these fully-formed contractile rings slid along the membrane of *cps1-191* cells at 36°C, as reported (Arasada and Pollard, 2014; Cortés et al., 2015). We shifted *cps1-191* cells from the permissive (25°C) to restrictive (36°C) temperature on the microscope to determine the time required for the phenotype to manifest. When the SPBs separated within 30

min of the temperature shift, furrow ingression was normal. If SPB separation occurred >30 min after the shift, furrows did not form normally (Fig S1A).

We made a strain with just the *bgs1*^{D277N} mutation in a wild-type background and found that furrowing progressed 3-fold faster (median 0.06 µm/min) than in *cps1-191* cells. Nevertheless, these *bgs1*^{D277N} cells had a growth defect at 36°C similar to the *cps1-191* strain (Fig. S1B). Both *bgs1*^{D277N} and *cps1-191* cells lysed frequently during imaging (Fig. S1D), which caused the growth defect at 36°C on solid medium. None of the *bgs1*$^{+}$ strains we examined lysed during observations. The lysis frequency varied substantially between replicate samples, suggesting that this phenotype is extremely sensitive to minute environmental differences. Consistent with this hypothesis, the osmotic stabilizer sorbitol partially rescued the growth of *cps1-191* and *bgs1*^{D277N} cells at 36°C (Fig. S1C).

The cps1-191 *strain carries a large number of mutations*

We sequenced the complete genome of the *cps1-191* strain. Comparison to the *S. pombe* reference genome obtained from PomBase (Wood et al., 2002; Lock et al., 2019) revealed 384 unique mutations, 271 of which were transition mutations consistent with the nitrosoguanidine mutagenesis used to generate the strain (Balasubramanian et al., 1998) (Fig. 2A). Ten of these transition mutations substituted amino acids in eight genes, including the reported *bgs1*^{D277N} mutation, located across all three chromosomes (Fig. 2B, Table 1).

Mutations in the Mto1/Mto2 complex synthetically interact with the bgs1^{D277N} *mutation*

To determine which mutations contribute to the *cps1-191* phenotype, we examined the PomBase annotations for each protein-coding gene with a substitution mutation (Table 1), looking for roles in cell cycle regulation or cytokinesis (Lock et al., 2019). Two of the eight affected genes, Mto2 and Nup40, met this criterion. Next, we took advantage of the fact that we saved multiple progeny from crosses generating *cps1-191* strains with labeled rings and SPBs. We measured the furrowing rates at 36°C and determined the *mto2* and *nup40* mutation status for each of these strains. Only presence of the *mto2*^{S338N} mutation correlated with the slowest furrowing rate observed for *cps1-191* (Table S1). The *mto2*^{S338N} mutation was also particularly interesting due to previous work linking Mto2 to the cytokinetic ring (Samejima et al., 2010).

Combining the *bgs1*^{D277N} and *mto2*^{S338N} mutations in a wild-type background reproduced the slow constriction rate of *cps1-191* (Fig. 1A, C). The Mto2 C terminus is highly phosphorylated (Borek et al., 2015), so we tested if the absence of phosphorylation at S338 caused the synthetic interaction with *bgs1*^{D277N}. Neither S338C, which precludes phosphorylation of S338, nor the [24A] strain with 24 phosphorylated serines mutated to alanines (Borek et al., 2015), constricted as slowly as the *bgs1*^{D277N} *mto2*^{S338N} or *cps1-191* mutants, but instead resembled the *bgs1*^{D277N} strain with the single mutation (Fig. 1A, C).

Mto2 contributes to the formation and regulation of non-SPB MTOCs in *S. pombe* through interactions with its binding partner Mto1 (Sawin and Tran, 2006). Neither *mto1*$^{+}$ nor *mto2*$^{+}$ are essential genes, and mutations of *mto1*$^{+}$ are more severe than mutations of *mto2*$^{+}$ (Sawin et al., 2004; Venkatram et al., 2005). In a *bgs1*$^{+}$ background with Rlc1-tdTomato to label contractile rings and Pcp1-mEGFP to label SPBs, all mutant strains of *mto1* and *mto2* formed furrows at the wild-type rate with cytokinesis timelines similar to wild-type cells (Fig. 1D, E). Deletion of Mto1, but not Mto2, slowed furrowing in a *bgs1*^{D277N} strain to the rate observed in *cps1-191* cells, while *mto2Δ* cells exhibited an intermediate phenotype (Fig. 1C). Therefore, the *bgs1*^{D277N} mutation sensitizes cells with a compromised Mto1/Mto2 complex.

Mitotic microtubules are disrupted in mto1Δ *and* mto2^{S338N} *cells*

We investigated the microtubule cytoskeleton in *mto1Δ* and *mto2*^{S338N} cells to determine common phenotypes that may affect furrow ingression. Over the course of spindle elongation in wild-type cells each SPB nucleated multiple, short-lived astral microtubules with a median duration of 20 s (n = 175 microtubules) (Fig. 3A, S2A). The *mto2*^{S338N} strain produced fewer astral microtubules than normal, and most SPBs nucleated no astral microtubules in *mto1Δ*, as reported (Sawin et al., 2004)(Fig. 3B, C). We measured the numbers of microtubules nucleated by SPBs only during anaphase B, to avoid intra-nuclear "astral" microtubules nucleated prior to this stage, which may not be affected by *mto1* loss (Zimmerman et al., 2004). As reported (Sawin et al., 2004), we did not observe PAA formation in *mto1Δ* cells, but the PAA formed at the normal time in *mto2*^{S228N} cells.

The time at which the spindle began to disassemble after reaching its maximum length, referred to as spindle breakage, occurred later than normal in both the *mto2*^{S338N} and *mto1Δ*

strains (Fig. 3D, $p < 0.05$ by pairwise K-S tests with Bonferroni correction). Both spindle breakage and initial formation of the PAA occur during the ring maturation stage (Fig. S2C).

Although the cytokinetic timelines of *mto2*^{S338N} and *mto1Δ* cells were indistinguishable from wild-type cells at 36°C (Fig. 2E), GFP-Atb2 expression caused synthetic phenotypes with these mutations. Ring assembly was slightly delayed in *mto2*^{S338N} and *mto1Δ* cells carrying GFP-Atb2 compared with wild-type cells bearing GFP-Atb2 (Fig. 3E, $p < 0.05$ by pairwise K-S tests with Bonferroni correction, $n \geq 21$ cells). Completion of ring constriction was also delayed in *mto1Δ* cells in this experiment. This substantiates that the *mto1Δ* and *mto2*^{S338N} mutations perturb cytokinesis when combined with additional stressors. We believe that the effects we observe on astral microtubule nucleation are not an artifact of GFP-Atb2 expression, as they are consistent with *mto1Δ* and *mto2Δ* microtubule-nucleation defects shown by immunofluorescence (Sawin et al., 2004; Janson et al., 2005; Samejima et al., 2005).

We considered whether PAA microtubules nucleated by the Mto1/Mto2 complex might promote trafficking of vesicles with Bgs1 to the division site and cause the synthetic effects of combining a Bgs1 mutation with compromised microtubule-nucleation machinery. However, the number of Bgs1 molecules recruited to the equator during cytokinesis of *bgs1*$^{+}$ *mto1Δ* and *bgs1*$^{+}$ *mto2*^{S338N} cells did not differ from wild-type cells (Fig. S2D), refuting this trafficking hypothesis.

mto1Δ *and* mto2^{S338N} *cells do not exhibit SIN phenotypes*

We wondered whether the septation initiation network (SIN) signaling pathway operates normally in the *mto1Δ* and *mto2*^{S338N} mutants. The SIN (Hippo in humans and MEN in budding yeast) drives formation of the contractile ring and cytokinesis (Simanis, 2015). Hyperactivation promotes septum formation during interphase (Minet et al., 1979), while low SIN activity results in unstable contractile rings and unreliable cytokinesis, promoting formation of multinucleate cells (Mitchison and Nurse, 1985; Dey and Pollard, 2018). We rarely observed the formation of binucleate interphase cells in the *mto1Δ* mutant cells and never in *mto2*^{S338N} cells. The *mto1Δ* cells have defects in nuclear positioning (Zimmerman and Chang, 2005), so both nuclei occasionally migrate into one daughter compartment after the contractile ring forms, resulting in one binucleate and one anucleate daughter cell. Contractile rings in these cells formed at the correct time in mitosis and did not disassemble. Early in mitosis, the SIN kinase Cdc7 first localizes to both SPBs and then to only one SPB during anaphase B (Sohrmann et al., 1998).

Cdc7 localizes to one SPB in *cps1-191* cells with an unconstricted ring, which suggests normal SIN activity (Liu et al., 1998).

Cytokinetic rings in *cps1-191*, *bgs1*^{D277N}, and *mto2*^{S338N} cells are so stable that we never observed one disassemble, suggesting that the SIN activity is normal. In 3 of 189 *mto1Δ* cells examined, a ring formed without SPB separation. One of these cells carried GFP-Atb2 and the microtubules emanated from the SPB in an aster-like array, so the ring likely formed at the normal time during a failed mitosis, rather than during interphase (Fig S2D). One of these three rings was subsequently disassembled, so SIN activity may be abnormal in a very small fraction of *mto1Δ* cells. The extremely low penetrance of ring formation without SPB separation and subsequent ring disassembly in *mto1Δ* cells (<0.5% of cells) prevented us from undertaking a quantitative examination of SIN activity in this population. The absence of this phenotype in any of the strains bearing *mto1*$^{+}$ (n = 844 cells) suggests that SIN defects are not what sensitizes *mto1Δ* or *mto2*^{S338N} cells to the loss of Bgs1 function.

mto1Δ *modulates the effects of salt stress on cytokinesis*

Acute salt stress produced by addition of 0.6 M KCl to rich medium (YE5S) causes a delay in ring constriction particularly in cells lacking *myp2*, which encodes one of two type-II myosins in fission yeast (Bezanilla et al., 1997; Okada et al., 2019). Myp2 recruits Mto1 to the ring and is required to generate the PAA (Samejima et al., 2010). We hypothesized that if loss of Mto1 at the equator causes sensitization to salt stress in *myp2Δ* cells, we would observe the same effect of salt stress in *mto1Δ* and *mto2*^{S338N} cells. We found that 0.6 M KCl also decreases the rate of ring constriction in minimal medium (EMM5S) in wild-type, *mto2*^{S338N}, and *mto1Δ* cells (Fig. 4A). Surprisingly, rings in *mto1Δ* cells constricted faster than in wild-type cells in the presence of this stress, though still more slowly than in the absence of KCl, so rings completed constriction earlier than in the other two strains in the presence of KCl (Fig. 4C). However, the *mto1Δ* and *mto2*^{S338N} phenotypes are distinct from the *myp2Δ* phenotype under salt stress (Okada et al., 2019), so the loss-of-function phenotypes differ for the Mto1/Mto2 complex and Myp2.

The mto1Δ *and* mto2^{S338N} *cells have high Rho-GTP at the cleavage site*

To explore one of many possible pathways influenced by the defects in astral microtubules, we localized *S. pombe* Rho1-GTP using the Pkc1(HR1-C2)-mEGFP biosensor (Davidson et al.,

2015). This probe, derived from *Saccharomyces cerevisiae* Pkc1, contains Rho-GTP binding HR1 domains and a plasma-membrane targeting C2 domain fused to mEGFP (Kono et al., 2012). The fluorescence of this probe is the same when free or bound to Rho-GTP, so it can measure the local accumulation but not the total active Rho-GTP. Binding of biosensors can compromise functions of the target protein, so expression of the biosensor may perturb cytokinesis if Rho1-GTP regulates furrow formation. To limit perturbation, the thiamine-repressible *3nmt1* promoter controlled the expression of Pkc1(HR1-C2)-mEGFP and cells were grown medium lacking thiamine (i.e. inducing conditions) for only ~15 h prior to imaging, the minimum time for maximum expression (Maundrell, 1990). Conveniently, expression from the *P3nmt1* promoter was highly variable, giving cells with a range of concentrations of Pkc1(HR1-C2)-mEGFP.

Expression of the biosensor consistently decreased the ring constriction rate of wild-type, $mto2^{S338N}$, and *mto1Δ* cells (Fig. 4F), delaying completion of constriction for all genotypes. On the other hand, the constriction rates were not strongly correlated with Pkc1(HR1-C2) expression level (by Spearman correlation test, which was used because Pkc1(HR1-C2) expression levels were not normally distributed)(Fig. S2B). The cytokinetic timelines of wild-type and $mto2^{S338N}$ cells were statistically indistinguishable with and without Pkc1(HR1-C2), but expression of the biosensor delayed further both the duration of maturation and completion of constriction in *mto1Δ* cells ($p < 0.05$ by K-S test with Bonferroni correction)(Fig. 4D, E).

Fluorescence microscopy of Pkc1(HR1-C2)-mEGFP confirmed that Rho1-GTP concentrates at cell tips during interphase and at the cytokinetic furrow in wild-type cells (Fig. 5A, Movie S1) as reported (Davidson et al., 2015). Fig. 5A shows a representative $mto1^{+}$ $mto2^{+}$ cell with the same pattern of Pkc1(HR1-C2)-mEGFP localization observed in *mto1Δ* and $mto2^{S338N}$ cells. Pkc1(HR1-C2)-mEGFP also concentrated at other cortical locations; this ectopic localization was much more frequent in $mto2^{S338N}$ (49%) and *mto1Δ* (46%) mutants than in wild-type (23%) cells (Fig. 5B, Movies S2, S3.). The $bgs1^{D277N}$ cells expressing Pkc1(HR1-C2)-mEGFP grew very poorly at 36°C, so we were unable to quantify Rho activity. This genetic interaction suggests that *cps1-191* cells are more sensitive to the effects of the Rho biosensor on Rho1 function.

The Pkc1(HR1-C2)-mEGFP signal peaked at the cleavage site during furrow ingression (Fig. 5C), followed by a brief decrease and second peak during cell separation (single light blue

data point in Fig. 5C). The normalized peaks of Pkc1(HR1-C2)-mEGFP fluorescence during cytokinesis and at separation were more intense in *mto2*^{S338N} and *mto1Δ* cells than wild-type cells (Fig. 5D). Furthermore, the cytokinesis peak of Pkc1(HR1-C2)-mEGFP fluorescence was prolonged in *mto1Δ* cells (Fig. 5E).

Discussion

Since its description in 1999, the *cps1-191* strain has been the gold standard to generate *S. pombe* cells arrested with stable, unconstricting actomyosin rings. We find a more nuanced phenotype that depends on both the originally-identified *bgs1*^{D277N} mutation and an additional mutation, *mto2*^{S338N}. Caution is advised when interpreting published results from *cps1-191* experiments examining the "arrest" phenotype, particularly those that required crossing the *cps1-191* strain with other strains, as the *mto2*^{S338N} mutation may no longer be present with the *bgs1*^{D277N} mutation. The *bgs1* and *mto2* loci are both on Chromosome II but are ~2 Mb apart. Isolating progeny that undergo a recombination event between these genes is common in our hands. A *cps1-191 mto2Δ* double mutant was previously examined, though the authors were presumably unaware of the *mto2*^{S338N} mutation in the *cps1-191* strain (Venkatram et al., 2005). However, we found that *bgs1*^{D277N} *mto2*^{S338N} had a more severe phenotype than *bgs1*^{D277N} *mto2Δ*. The molecular basis of this difference is currently unknown.

Microtubule depolymerization in metazoan cells increases Rho-GTP levels and has profound effects on the actin cytoskeleton (Zhang et al., 1997; Danowski, 1989; Liu et al., 1998; Enomoto, 1996). Astral microtubule plus ends carry the Aurora A activator TPXL-1 to the cortex, where it inactivates Rho in *C. elegans* embryos (Mangal et al., 2018). Binding to microtubules inactivates Rho GEF-H1 in mammalian cells, so depolymerizing microtubules releases this GEF and thereby increases Rho activity (Krendel et al., 2002). Cells lacking Mto1 produce no PAA microtubules. The loss of the PAA microtubules in addition to fewer astral microtubules may explain why *mto1Δ* cells recruit more Rho1-GTP to the division site than *mto2*^{S338N} cells, which form a normal PAA and have an intermediate astral microtubule number. While *S. pombe* has no clear homologs for either TPXL-1 or GEF-H1, the high and prolonged Rho activity at the cell equator in *mto2*^{S338N} and *mto1Δ* cells suggests mitotic microtubules may also inhibit cortical Rho in fission yeast.

When in the active, GTP-bound state, RhoA in metazoan cells localizes to the cell cortex and GDP-dissociation inhibitors (GDIs) sequester GDP-bound GTPases in the cytoplasm (Michaelson et al., 2001). Membrane-localization through the C-terminal CAAX motif is thought to increase Rho activity by increasing the likelihood of activation by GEFs. This hypothesis is supported by the observation that specific localization of the p63RhoGEF to the plasma membrane is sufficient to drive RhoA activation and its downstream effects (van Unen et al., 2015). Therefore, we expect that the pool of Rho1-GTP we detect with the plasma-membrane localized Pkc1(HR1-C2)-mEGFP biosensor represents the relevant pool of active Rho1.

The *mto1Δ* and *mto2*^{S338N} cells recruit excess Rho-GTP to the division site, but an additional insult (e.g. Bgs1 mutation, salt stress, Rho biosensor or GFP-Atb2 expression) is required to sensitize these cells and produce a furrow ingression phenotype. Why cells tolerate excess Rho-GTP so well, and how increased Rho-GTP modulates furrow ingression under multiple stressors are unclear. Much more work is required to assess which of the Rho1 regulators contribute to the observed hyperactivation and exactly how this influences furrow ingression. Many Rho1 regulators are known to be involved in septation, but how microtubules might regulate any of these proteins is currently unclear.

An additional mystery is why combination of Mto1/Mto2 mutations with the *bgs1*^{D227N} mutation decreases the furrowing rate while salt stress increases the furrowing rate, particularly because these mutants recruit normal levels of Bgs1 to the division site. Cells depleted of Bgs1 using the *nmt1* promoter and *cps1-191* cells exhibit abnormally-thick cell walls and secondary septa, suggesting that other glucan synthases attempt to compensate for the loss of Bgs1 activity (Cortés et al., 2007; 2015; Sethi et al., 2016). Excess Rho1-GTP at the division site may compromise the activity of these enzymes.

Changing Rho expression perturbs the levels of other GTPases (e.g. Rac, Cdc42) through competition for shared GDIs in mammalian cells, and it has been proposed that changes in the activity of Rho could also affect other GTPases through this mechanism (Boulter et al., 2010). *S. pombe* has a single Rho GDI, Gdi1, so an altered Rho1-GDP/GTP balance may change the amount of Gdi1 available to interact with other GTPases involved in cytokinesis such as Cdc42, Rho2, and Rho4. Rho1 activates Bgs1 (primary septum) and Bgs4 (secondary septum), but Rho2 regulates Ags1 (secondary septum). In *bgs1*^{D277N} *mto2*^{S338N} or *bgs1*^{D277N} *mto1Δ* cells, increased Rho1 at the division site may perturb Rho2 and Ags1 activity, compromising the ability of cells

to compensate for lack of Bgs1 and causing even slower furrow ingression than the *bgs1*^{D277N} substitution alone.

Our data suggest that mitotic microtubules, and astral microtubules in particular, participate in signaling to the division machinery and regulate furrow ingression. The SPB is known to serve as a hub for cell cycle signals—e.g. the SIN—and proteins localizing to the SPB throughout mitosis serve as markers for progression of the cell cycle (Tatebe et al., 2001; Grallert et al., 2004). Two, non-mutually-exclusive options for astral microtubule involvement in this signaling are facilitating recruitment of known cell-cycle regulators to the SPB and serving as signaling platforms in their own right. Much more research is required to determine exactly how microtubules interact with the three requirements for furrow formation: an intact contractile ring; a signal originating from the cell cycle clock; and initiation of septum synthesis.

Our work demonstrates that crosstalk between microtubules and the furrow machinery mediated by Rho is conserved more broadly than previously thought and raises many intriguing questions regarding the molecular details of this communication in fungal cells. During cytokinesis of metazoan cells, RhoA regulates the location of the cytokinetic ring, activates formins for cytokinetic ring assembly, promotes myosin activity through Rho-associated protein kinase (ROCK), and promotes midbody ring maturation through Citron kinase (Pollard, 2017; El-Amine et al., 2019). Ring positioning is achieved through other mechanisms in fission yeast (Pollard, 2017), but Rho1 contributes to full activation of the SIN to drive ring formation (Alcaide-Gavilán et al., 2014) and has essential roles in septum synthesis through its interaction with glucan synthases (Arellano et al., 1996). This suggests that Rho signaling is an ancient mechanism for coordinating cytoskeletal elements and that during the divergence from the LECA (the last eukaryote common ancestor) Rho signaling has been adapted for a range of functions to regulate cytokinesis.

Acknowledgments

Research reported in this publication was supported by National Institute of General Medical Sciences of the National Institutes of Health under award number R01GM026132 and an NRSA fellowship (F32GM125193) to S. Dundon. The content is solely the responsibility of the authors and does not necessarily represent the official views of the National Institutes of Health. The authors thank M. Balasubramanian, M. Das, and D. McCollum, for useful discussions; F. Chang,

M. C. King, J. C. Ribas, K. E. Sawin, and J.-Q. Wu for generously sharing *S. pombe* strains; J. Berro and R. Fernandez for assistance with CRISPR; R. M. Dundon and T. J. Straub for assistance with genome analysis. The authors declare no competing financial interests.

Methods and Materials

Growth conditions and strain construction

Table S2 lists the *S. pombe* strains used in this work. Oligonucleotide primers were from Millipore Sigma. Restriction enzymes were from New England BioLabs. Plasmid purification was performed using an E.Z.N.A Plasmid Mini Kit (Omega Bio-tek) with Miraprep modifications (Pronobis et al., 2016). The Keck DNA Sequencing Lab of Yale University performed routine DNA sequencing. All cloning was done with high-efficiency NEB 5-alpha Competent *E. coli* from New England BioLabs. Standard methods were used for genetic crosses (Moreno et al., 1991).

mto2^{S338N}*:KanMX6* and *mto2*^{S338C}*:KanMX6* strains of *S. pombe* were generated by homologous integration (Bähler et al., 1998). First, pFA6a-mto2^{S338N}-C-KanMX6 was generated. A 245-base fragment of the end of the *mto2* coding sequence was amplified from *cps1-191* (containing the *mto2*^{S338N} mutation) with flanking homology to the pFA6a vector using the Expand^{TM} High Fidelity PCR system (Millipore Sigma). The vector backbone was amplified from pFA6a-GFP-KanMX6 using Phusion polymerase (New England BioLabs). Both PCR reactions were digested with DpnI and purified using an E.Z.N.A Cycle Pure Kit (Omega Bio-tek). pFA6a-mto2^{S338N}-C-KanMX6 was generated using NEBuilder HiFi DNA Assembly Master Mix (New England BioLabs) in an assembly containing 5 fmol of each fragment. The *mto2*^{S338N} segment was verified by sequencing. pFA6a-mto2^{S338C}-C-KanMX6 was generated by site-directed mutagenesis. Mutagenic primers were used to amplify pFA6a-mto2^{S338N}-C-KanMX6 using the Expand High Fidelity PCR system (Millipore Sigma). The PCR product was digested with DpnI and transformed into NEB 5-alpha Competent *E. coli*. The *mto2*^{S338C} segment was verified by sequencing.

PCR-based homologous integration cassettes were amplified using the Expand^{TM} High Fidelity PCR system (Millipore Sigma) from the appropriate plasmid with 80 bp flanking homology to replace the 3' end of *mto2* (primers designed with PPPP at www.bahlerlab.info/resources/)(Bähler et al., 1998). Lithium acetate transformation was used to

introduce 5-10 µg of integration cassette DNA (Murray et al., 2016). Integration at the correct locus was verified by colony PCR using LongAmp *Taq* 2X Master Mix (New England BioLabs), and the *mto2* gene was sequenced in its entirety to verify the S338N or S338C point mutations.

The *bgs1*^{D277N} strain was generated by CRISPR (Fernandez and Berro, 2016). A two-step PCR was used to assemble pUR19-adh1-Cas9-rrk1-sgRNA:Fex1^{+} with a guide sequence targeting *bgs1* using Q5 High-Fidelity polymerase (New England BioLabs). pUR19-adh1-Cas9-rrk1-sgRNA:Fex1^{+} and a 400-bp repair guide fragment containing the *bgs1*^{D277N} mutation were introduced into *fex1Δ fex2Δ S. pombe* cells by lithium acetate transformation (Murray et al., 2016). The *bgs1* gene was sequenced in its entirety to verify the *bgs1*^{D277N} mutation.

Whole-genome sequencing

S. pombe genomic DNA was isolated using a *Quick*-DNA Fungal/Bacterial Miniprep kit and purified by a Genomic DNA Clean & Concentrator-25 kit (both from Zymo Research). Genomic DNA was sequenced on a NovaSeq 6000 (Illumina) with 150 bp paired reads at the Yale Center for Genome Analysis. Sequence data quality was examined using FastQC v 0.11.7 (Babraham Bioinformatics). The *S. pombe* reference genome was downloaded from PomBase (Lock et al., 2019) and reads were aligned using MagicBLAST (Zhang et al., 2015). Aligned reads were sorted, duplicates removed, and indexed using SAMtools (Li et al., 2009). Deviations from the reference genome were identified using Pilon (Walker et al., 2014), and alignments were viewed using IGV 2.4.10 (Robinson et al., 2017). Identified mutations were cross-referenced with PomBase to determine location, eliminate previously-reported variants, and identify protein-coding mutations (Lock et al., 2019).

Microscopy

Cells were grown in 50 mL baffled flasks in exponential phase at 25°C in YE5S (rich) medium for 24 h, then washed into EMM5S (low-fluorescence) medium for an additional 12 h. For experiments at 36°C, the culture was shifted to 36°C 2 h prior to mounting and imaging. To image, cells were isolated by centrifugation at 2300 x g for 30 s, washed with fresh EMM5S, and resuspended at ~20-fold higher concentration than in culture. Then 1.5-2.0 µL of concentrated cells were mounted on an EMM5S + 2% agarose pad freshly poured on a Therminator block (Davies et al., 2014) and a 24 x 50 mm no 1.5 coverslip was applied (Globe Scientific). Then 150

μL of EMM5S was injected beneath the coverslip in contact with the agarose pad and the edges of the chamber were sealed using VALAP to reduce shrinkage of the pad. For salt stress experiments, cells at 25°C were washed and resuspended in EMM5S + 0.6 M KCl, then immediately mounted on an EMM5S + 0.6 M KCl + 2% agarose pad on a Therminator block and imaged at 25°C.

Cells were visualized using an Olympus IX-71 microscope with a 100×/numerical aperture (NA) 1.4 Plan Apo lens (Olympus) and a CSU-X1 (Andor Technology) confocal spinning-disk confocal system equipped with an iXON-EMCCD camera (Andor Technology). OBIS 488 nm LS 20 mW and OBIS 561 nm LS 20 mW lasers (Coherent) for excitation. The desired temperature was maintained during acquisition using a home-built version of the Therminator (Davies et al., 2014). Images were acquired using Micromanager 1.4 (Edelstein et al., 2014).

Acquisition settings for Pcp1-mEGFP Rlc1-tdTomato: 12 Z-slices were acquired with 0.5 μm spacing; 22 μW 561 nm laser power and 50 ms exposures; 35 μW 488 laser power and 50 ms exposures (power measured at the objective). An emission filter suitable for both tdTomato and mEGFP fluorescence was used to reduce the number of filter changes. All *bgs1*$^{+}$ cells were imaged at 4 XY positions and 1-min intervals. Cells carrying *bgs1*^{D277N} were imaged at 20 XY positions and 5-min intervals.

Acquisition settings for Rlc1-tdTomato Sfi1-mCherry mEGFP-Atb2: For cytokinesis timelines to determine the timing of spindle breakage, 12 Z-slices were acquired with 0.5 μm spacing at 3 XY positions and 1-minute intervals using 150 ms exposures with 32 μW 561 nm laser power and 200 ms exposures with 89 μW 488 laser power at the objective. Separate emission filters were used for tdTomato/mCherry and mEGFP fluorescence to avoid bleed through of the fluorophores with different spectral characteristics. To measure astral microtubule numbers and longevities, only mEGFP-Atb2 was imaged using 89 μW 488 laser power and 200 ms exposures of 10 Z-slices with 0.5 μm spacing at one XY position at 10-s intervals.

Acquisition settings for GFP-Bgs1 Rlc1-tdTomato Sfi1-mCherry: 12 Z-slices with 0.5 μm spacing were acquired at 3 XY positions and 1-min intervals using 150 ms exposures with 32 μW 561 nm laser power and 100 ms exposures with 89 μW 488 laser power at the objective. Separate emission filters were used for tdTomato/mCherry and mEGFP fluorescence to avoid bleed through of the fluorophores with different spectral characteristics. Strains bearing GFP-

tagged proteins for the calibration curve were imaged under identical conditions. For camera noise correction, 100 images were acquired with 100 ms exposures and the shutter closed; for uneven illumination correction, dilute fluorescein was mounted on a 2% agarose EMM5S pad on the Therminator and 100 images were acquired using 50 ms exposures with 34 μW 488 laser power.

Image Analysis

All image visualization and analyses were done using Fiji (Schindelin et al., 2012). Macros used for processing can be downloaded from https://github.com/SDundon/ImageJ-Processing-Macros. Prior to analysis, the contrast of each image was adjusted so that the black point was 5% below extracellular background signal and the white point was 20% above maximum signal intensity. Representative images were selected based on similarity to median values of each data set.

Constriction rates and cytokinesis timeline measurements: Maximum-intensity projections were produced for each time-lapse acquisition and a kymograph was first produced for each ring. If necessary, the StackReg plugin (Thévenaz et al., 1998) was used to register images across all time points. A line was drawn parallel to the ring, the "reslice" tool in Fiji used, and the resliced image was maximum-intensity projected to create a kymograph. Ring circumference for each time point was calculated using the 180912_AutoCircum.ijm macro. Circumference was plotted against time as a scatter plot in Microsoft Excel, and a linear trendline fit to the slope to calculate the constriction rate. For analysis of cells bearing the *bgs1*^{D277N} mutation (including *cps1-191*), cells were excluded from analysis if SPB separation occurred > 2 h after the start of acquisition. We found that rings formed after this time always constricted at an even slower rate, most likely due to effects of phototoxicity.

Cytokinesis milestones were defined as follows: "SPB separation" is the first frame in which two SPBs labeled with Pcp1-mEGFP could be resolved; "Complete assembly" is the first frame in which no Rlc1-tdTomato-labeled nodes were visible adjacent to the ring, because all had coalesced at the equator; "Constriction onset" is the first frame in which the Rlc1-tdTomato-labeled ring was smaller than its initial diameter and continued to decrease in size; "Constriction complete" is the frame in which the Rlc1-tdTomato signal reached its smallest size at the end of constriction. All milestones were temporally aligned with SPB separation set as time 0 and plotted as cumulative distributions. Spindle breakage was defined as the first time point in which

there was no longer a single microtubule structure marked with GFP-Atb2 connecting the two SPBs. PAA appearance was defined as the first frame in which microtubules appeared at the equator distinct from the mitotic spindle.

Astral microtubule measurements: Astral microtubules were considered to be the same structure across consecutive frames (10 s intervals) if they a) originated from the same SPB and b) were oriented in the same direction ± 45° relative to the SPB in consecutive frames (Fig. 3A). The number of astral microtubules that originated from a single SPB during anaphase B was determined to exclude the intra-nuclear "astral" microtubules that form during earlier phases of mitosis (Zimmerman et al., 2004).

Rho biosensor and GFP-Bgs1 measurements: A ROI was selected for bleach correction reference using the following criteria: 1) must stay within the boundaries of one cell for the duration of the acquisition. 2) must be located within a cell that does not divide for the duration of the movie (to prevent differences in cytosolic concentration due to recruitment to the division site); 3) Pcp1-mEGFP-marked SPB must never enter the ROI. The same ROI was used for bleach correction of all channels. Bleach correction was conducted using the Fiji plugin for Exponential Fitting Method for the Bleach Correction. The intensity from all 12 Z-slices (0.5 µm apart) was then summed.

Rho biosensor measurements: Prior to analysis, the contrast of each image was adjusted so that the black point was 5% below extracellular background signal and the white point was 20% above maximum signal intensity of Pcp1-mEGFP, which was more consistent than pkc1(HR1-C2)-mEGFP signal. As previously observed, expression from the *3nmt1* promoter was highly variable. Therefore, cells were analyzed that had an average pkc1(HR1-C2)-mEGFP pixel intensity of >175,000 A.U. at SPB separation. This was calculated by drawing a spline-fit polygon ROI around the cell at the last time point prior to SPB separation. The integrated density was measured for this ROI, as well as a circular ROI covering the SPB. The SPB integrated density was subtracted from the cellular integrated density, and this value divided by the cell area with SPB area subtracted. This value (175,000 arbitrary units) was selected because cells of all genotypes below this threshold were found to have very low Peak Rho/Interphase Rho ratio values with a very different standard deviation than cells above this threshold. We reasoned that cells below this threshold express insufficient pkc1(HR1-C2)-mEGFP to enable reliable measurement of active Rho enrichment at the cell equator. After elimination of cells below this

threshold, the data were homoscedastic when the ratio was plotted against average pixel intensity.

To calculate the Peak Rho/Interphase Rho ratio, a 3.75 x 1.95 μm ROI was positioned with the cytokinetic ring in the center (long axis to match the cell width). The integrated density was measured for this ROI for each time point. These values were divided by the integrated density of this ROI for the time point immediately prior to SPB separation to normalize the intensity by Pkc1(HR1-C2)-mEGFP expression. Normalized intensity was plotted against time using Microsoft Excel, all time points in which the SPB was located within the ROI were excluded. To measure peak duration, the peak fluorescence start was defined as the last time point of consistent signal increase across >3 time points. Peak end was defined as the last time point prior to consistent signal decrease below the peak start value across >3 time points. For cytokinesis peak signal, the maximum ratio between these points was determined. For separation peak signal, the maximum normalized signal within two time points of cell separation was determined.

Measurements of Bgs1 molecule numbers: Bleach-corrected summed intensity images were corrected for camera noise and uneven illumination. To generate the calibration curve, a spline-fit polygon ROI was drawn around wild-type (unlabeled) cells and the average intensity in the ROI was measured (n = 74 cells). Subsequently, ROIs were similarly drawn around cells bearing seven different GFP-tagged proteins for the calibration curve (n > 65 cells). For each cell, the wild-type background fluorescence was subtracted and the integrated density was calculated. These integrated density measurements were plotted against the average number of molecules per cell for each protein reported in Wu and Pollard, 2005 and fit with a linear regression. A 1.0 μm by 3.75 μm (cell width) ROI was positioned to cover the equatorial GFP-Bgs1 signal and the integrated density measured from cell cycle time zero until 30 min past the completion of constriction. The same ROI was used to measure cytoplasmic GFP-Bgs1 signal adjacent to the ring at constriction onset. Cytoplasmic GFP-Bgs1 integrated density was subtracted from the equatorial signal until the onset of constriction. The average constriction rate and average ring size were used to calculate a correction factor for the progressively smaller cytoplasmic volume within the plane of the constricting ring, which was applied to the value of the cytoplasmic signal and subtracted from the equatorial signal until constriction completion.

Statistical analysis

All statistical tests were carried out in R (R Core Team, 2018). Plotting was done using tidyverse and ggbeeswarm packages (Wickham, 2017; Clarke and Sherrill-Mix, 2017), except for pie charts in Fig. 2, which were generated using Microsoft Excel.

References

Alcaide-Gavilán, M., A. Lahoz, R.R. Daga, and J. Jimenez. 2014. Feedback regulation of SIN by Etd1 and Rho1 in fission yeast. *Genetics*. 196:455–470.

Arasada, R., and T.D. Pollard. 2014. Contractile ring stability in *S. pombe* depends on F-BAR protein Cdc15p and Bgs1p transport from the Golgi complex. *Cell Rep*. 8:1533–1544.

Arellano, M., A. Durán, and P. Pérez. 1996. Rho 1 GTPase activates the (1-3)β-D-glucan synthase and is involved in *Schizosaccharomyces pombe* morphogenesis. *EMBO J*. 15:4584–4591.

Balasubramanian, M.K., D. McCollum, L. Chang, K.C. Wong, N.I. Naqvi, X. He, S. Sazer, and K.L. Gould. 1998. Isolation and characterization of new fission yeast cytokinesis mutants. *Genetics*. 149:1265–1275.

Bähler, J., J.Q. Wu, M.S. Longtine, N.G. Shah, A. McKenzie, A.B. Steever, A. Wach, P. Philippsen, and J.R. Pringle. 1998. Heterologous modules for efficient and versatile PCR-based gene targeting in *Schizosaccharomyces pombe*. *Yeast*. 14:943–951.

Bezanilla, M., S.L. Forsburg, and T.D. Pollard. 1997. Identification of a second myosin-II in *Schizosaccharomyces pombe*: Myp2p is conditionally required for cytokinesis. *Mol Biol Cell*. 8:2693–2705.

Borek, W.E., L.M. Groocock, I. Samejima, J. Zou, F. de Lima Alves, J. Rappsilber, and K.E. Sawin. 2015. Mto2 multisite phosphorylation inactivates non-spindle microtubule nucleation complexes during mitosis. *Nat Commun*. 6:1–16.

Boulter, E., R. Garcia-Mata, C. Guilluy, A. Dubash, G. Rossi, P.J. Brennwald, and K. Burridge. 2010. Regulation of Rho GTPase crosstalk, degradation and activity by RhoGDI1. *Nat Cell Biol*. 12:477–483.

Calonge, T.M., K. Nakano, M. Arellano, R. Arai, S. Katayama, T. Toda, I. Mabuchi, and P. Pérez. 2000. *Schizosaccharomyces pombe* Rho2p GTPase regulates cell wall α-glucan biosynthesis through the protein kinase Pck2p. *Mol Biol Cell*. 11:4393–4401.

Cheffings, T.H., N.J. Burroughs, and M.K. Balasubramanian. 2019. Actin turnover ensures uniform tension distribution during cytokinetic actomyosin ring contraction. *Mol Biol Cell*. 30:933–941.

Chen, Q., and T.D. Pollard. 2011. Actin filament severing by cofilin is more important for assembly than constriction of the cytokinetic contractile ring. *J Cell Biol*. 195:485–498.

Clarke, E., and S. Sherrill-Mix. 2017. Categorical scatter (Violin point) plots [R package ggbeeswarm version 0.6.0].

Coffman, V.C., A.H. Nile, I.-J. Lee, H. Liu, and J.-Q. Wu. 2009. Roles of formin nodes and myosin motor activity in Mid1p-dependent contractile-ring assembly during fission yeast cytokinesis. *Mol Biol Cell*. 20:5195–5210.

Cortés, J.C.G., E. Carnero, J. Ishiguro, Y. Sánchez, A. Durán, and J.C. Ribas. 2005. The novel fission yeast (1,3)β-D-glucan synthase catalytic subunit Bgs4p is essential during both cytokinesis and polarized growth. *J Cell Sci*. 118:157–174.

Cortés, J.C.G., M. Konomi, I.M. Martins, J. Muñoz, M.B. Moreno, M. Osumi, A. Durán, and J.C. Ribas. 2007. The (1,3)β-d-glucan synthase subunit Bgs1p is responsible for the fission yeast primary septum formation. *Mol Microbiol*. 65:201–217.

Cortés, J.C.G., M. Sato, J. Muñoz, M.B. Moreno, J.A. Clemente-Ramos, M. Ramos, H. Okada, M. Osumi, A. Durán, and J.C. Ribas. 2012. Fission yeast Ags1 confers the essential septum strength needed for safe gradual cell abscission. *J Cell Biol*. 198:637–656.

Cortés, J.C.G., N. Pujol, M. Sato, M. Pinar, M. Ramos, B. Moreno, M. Osumi, J.C. Ribas, and P. Pérez. 2015. Cooperation between Paxillin-like protein Pxl1 and glucan synthase Bgs1 is essential for actomyosin ring stability and septum formation in fission yeast. *PLoS Genet*. 11:e1005358.

Danowski, B.A. 1989. Fibroblast contractility and actin organization are stimulated by microtubule inhibitors. *J Cell Sci*. 93 (Pt 2):255–266.

Davidson, R., D. Laporte, and J.-Q. Wu. 2015. Regulation of Rho-GEF Rgf3 by the arrestin Art1 in fission yeast cytokinesis. *Mol Biol Cell*. 26:453–466.

Davies, T., S.N. Jordan, V. Chand, J.A. Sees, K. Laband, A.X. Carvalho, M. Shirasu-Hiza, D.R. Kovar, J. Dumont, and J.C. Canman. 2014. High-resolution temporal analysis reveals a functional timeline for the molecular regulation of cytokinesis. *Dev Cell*. 30:209–223.

Dey, S.K., and T.D. Pollard. 2018. Involvement of the septation initiation network in events during cytokinesis in fission yeast. *J Cell Sci*. 131:jcs216895.

Edelstein, A.D., M.A. Tsuchida, N. Amodaj, H. Pinkard, R.D. Vale, and N. Stuurman. 2014. Advanced methods of microscope control using μManager software. *J Biol Methods*. 1:e10.

El-Amine, N., S.C. Carim, D. Wernike, and G.R.X. Hickson. 2019. Rho-dependent control of the Citron kinase, Sticky, drives midbody ring maturation. *Mol Biol Cell*. 30:2185–2204.

Enomoto, T. 1996. Microtubule disruption induces the formation of actin stress fibers and focal adhesions in cultured cells: possible involvement of the Rho signal cascade. *Cell Struct. Funct.* 21:317–326.

Fernandez, R., and J. Berro. 2016. Use of a fluoride channel as a new selection marker for fission yeast plasmids and application to fast genome editing with CRISPR/Cas9. *Yeast*. 33:549–557.

Grallert, A., A. Krapp, S. Bagley, V. Simanis, and I.M. Hagan. 2004. Recruitment of NIMA kinase shows that maturation of the *S. pombe* spindle-pole body occurs over consecutive cell cycles and reveals a role for NIMA in modulating SIN activity. *Genes Dev*. 18:1007–1021.

Janson, M.E., T.G. Setty, A. Paoletti, and P.T. Tran. 2005. Efficient formation of bipolar microtubule bundles requires microtubule-bound gamma-tubulin complexes. *J Cell Biol*. 169:297–308.

Kono, K., Y. Saeki, S. Yoshida, K. Tanaka, and D. Pellman. 2012. Proteasomal degradation resolves competition between cell polarization and cellular wound healing. *Cell*. 150:151–164.

Krendel, M., F.T. Zenke, and G.M. Bokoch. 2002. Nucleotide exchange factor GEF-H1 mediates cross-talk between microtubules and the actin cytoskeleton. *Nat Cell Biol*. 4:294–301.

Laplante, C., J. Berro, E. Karatekin, A. Hernandez-Leyva, R. Lee, and T.D. Pollard. 2015. Three myosins contribute uniquely to the assembly and constriction of the fission yeast cytokinetic contractile ring. *Curr Biol*. 25:1955–1965.

Leong, S.L., E.M. Lynch, J. Zou, Y.D. Tay, W.E. Borek, M.W. Tuijtel, J. Rappsilber, and K.E. Sawin. 2019. Reconstitution of microtubule nucleation *in vitro* reveals novel roles for Mzt1. *Curr Biol*. 29:2199–2207.e10.

Li, H., B. Handsaker, A. Wysoker, T. Fennell, J. Ruan, N. Homer, G. Marth, G. Abecasis, R. Durbin, 1000 Genome Project Data Processing Subgroup. 2009. The Sequence Alignment/Map format and SAMtools. *Bioinformatics*. 25:2078–2079.

Li, Y., J.R. Christensen, K.E. Homa, G.M. Hocky, A. Fok, J.A. Sees, G.A. Voth, and D.R. Kovar. 2016. The F-actin bundler α-actinin Ain1 is tailored for ring assembly and constriction during cytokinesis in fission yeast. *Mol Biol Cell*. 27:1821–1833.

Liu, B.P., M. Chrzanowska-Wodnicka, and K. Burridge. 1998. Microtubule depolymerization induces stress fibers, focal adhesions, and DNA synthesis via the GTP-binding protein Rho. *Cell Adhes. Commun.* 5:249–255.

Liu, J., H. Wang, D. McCollum, and M.K. Balasubramanian. 1999. Drc1p/Cps1p, a 1,3-β-glucan synthase subunit, is essential for division septum assembly in *Schizosaccharomyces pombe*. *Genetics*. 153:1193–1203.

Lock, A., K. Rutherford, M.A. Harris, J. Hayles, S.G. Oliver, J. Bahler, and V. Wood. 2019. PomBase 2018: user-driven reimplementation of the fission yeast database provides rapid and intuitive access to diverse, interconnected information. *Nucleic Acids Res*. 47:D821–D827.

Loo, T.-H., and M. Balasubramanian. 2008. *Schizosaccharomyces pombe* Pak-related protein, Pak1p/Orb2p, phosphorylates myosin regulatory light chain to inhibit cytokinesis. *J Cell Biol*. 183:785–793.

Mangal, S., J. Sacher, T. Kim, D.S. Osório, F. Motegi, A.X. Carvalho, K. Oegema, and E. Zanin. 2018. TPXL-1 activates Aurora A to clear contractile ring components from the polar cortex during cytokinesis. *J Cell Biol*. 217:837–848.

Maundrell, K. 1990. nmt1 of fission yeast. A highly transcribed gene completely repressed by thiamine. *J. Biol. Chem.* 265:10857–10864.

Michaelson, D., J. Silletti, G. Murphy, P. D'Eustachio, M. Rush, and M.R. Philips. 2001. Differential localization of Rho GTPases in live cells: regulation by hypervariable regions and RhoGDI binding. *J Cell Biol*. 152:111–126.

Minet, M., P. Nurse, P. Thuriaux, and J.M. Mitchison. 1979. Uncontrolled septation in a cell division cycle mutant of the fission yeast *Schizosaccharomyces pombe*. *J Bacteriol*. 137:440–446.

Mitchison, J.M., and P. Nurse. 1985. Growth in cell length in the fission yeast *Schizosaccharomyces pombe*. *J Cell Sci*. 75:357–376.

Morris, Z., D. Sinha, A. Poddar, B. Morris, and Q. Chen. 2019. Fission yeast TRP channel Pkd2p localizes to the cleavage furrow and regulates cell separation during cytokinesis. *Mol Biol Cell*. 30:1791–1804.

Moreno, S., A. Klar, and P. Nurse. 1991. Molecular genetic analysis of fission yeast Schizosaccharomyces pombe. *Meth. Enzymol.* 194:795–823.

Murray, J.M., A.T. Watson, and A.M. Carr. 2016. Transformation of *Schizosaccharomyces pombe*: lithium acetate/dimethyl sulfoxide procedure. *Cold Spring Harbor Protocols*. 2016:pdb.prot090969.

Nakano, K., R. Arai, and I. Mabuchi. 1997. The small GTP-binding protein Rho1 is a multifunctional protein that regulates actin localization, cell polarity, and septum formation in the fission yeast *Schizosaccharomyces pombe*. *Genes Cells*. 2:679–694.

Okada, H., C. Wloka, J.-Q. Wu, and E. Bi. 2019. Distinct roles of Myosin-II isoforms in cytokinesis under normal and stressed conditions. *ISCIENCE*. 14:69–87.

Pardo, M., and P. Nurse. 2003. Equatorial retention of the contractile actin ring by microtubules during cytokinesis. *Science*. 300:1569–1574.

Pelham, R.J., and F. Chang. 2002. Actin dynamics in the contractile ring during cytokinesis in fission yeast. *Nature*. 419:82-86.

Pollard, T.D. 2017. Nine unanswered questions about cytokinesis. *J Cell Biol*. 216:3007–3016.

Proctor, S.A., N. Minc, A. Boudaoud, and F. Chang. 2012. Contributions of turgor pressure, the contractile ring, and septum assembly to forces in cytokinesis in fission yeast. *Curr Biol*. 22:1601–1608.

Pronobis, M.I., N. Deuitch, and M. Peifer. 2016. The Miraprep: A protocol that uses a Miniprep kit and provides Maxiprep yields. *PLoS ONE*. 11:e0160509.

Roberts-Galbraith, R.H., J.-S. Chen, J. Wang, and K.L. Gould. 2009. The SH3 domains of two PCH family members cooperate in assembly of the *Schizosaccharomyces pombe* contractile ring. *J Cell Biol*. 184:113–127.

Roberts-Galbraith, R.H., M.D. Ohi, B.A. Ballif, J.-S. Chen, I. McLeod, W.H. McDonald, S.P. Gygi, J.R. Yates, and K.L. Gould. 2010. Dephosphorylation of F-BAR protein Cdc15 modulates its conformation and stimulates its scaffolding activity at the cell division site. *Mol Cell*. 39:86–99.

Robinson, J.T., H. Thorvaldsdóttir, A.M. Wenger, A. Zehir, and J.P. Mesirov. 2017. Variant review with the Integrative Genomics Viewer. *Cancer Res.* 77:e31–e34.

Samejima, I., P.C.C. Lourenco, H.A. Snaith, and K.E. Sawin. 2005. Fission yeast Mto2p regulates microtubule nucleation by the centrosomin-related protein Mto1p. *Mol Biol Cell*. 16:3040–3051.

Samejima, I., V.J. Miller, S.A. Rincón, and K.E. Sawin. 2010. Fission yeast Mto1 regulates diversity of cytoplasmic microtubule organizing centers. *Curr Biol*. 20:1959–1965.

Sawin, K.E., and P.T. Tran. 2006. Cytoplasmic microtubule organization in fission yeast. *Yeast*. 23:1001–1014.

Sawin, K.E., P.C.C. Lourenco, and H.A. Snaith. 2004. Microtubule nucleation at non-spindle pole body microtubule-organizing centers requires fission yeast centrosomin-related protein mod20p. *Curr Biol*. 14:763–775.

Schindelin, J., I. Arganda-Carreras, E. Frise, V. Kaynig, M. Longair, T. Pietzsch, S. Preibisch, C. Rueden, S. Saalfeld, B. Schmid, J.-Y. Tinevez, D.J. White, V. Hartenstein, K. Eliceiri, P. Tomancak, and A. Cardona. 2012. Fiji: an open-source platform for biological-image analysis. *Nat Meth*. 9:676–682.

Sethi, K., S. Palani, J.C.G. Cortés, M. Sato, M. Sevugan, M. Ramos, S. Vijaykumar, M. Osumi, N.I. Naqvi, J.C. Ribas, and M. Balasubramanian. 2016. A new membrane protein Sbg1 links the contractile ring apparatus and septum synthesis machinery in fission yeast. *PLoS Genet*. 12:e1006383–30.

Simanis, V. 2015. Pombe's thirteen - control of fission yeast cell division by the septation initiation network. *J Cell Sci*. 128:1465–1474.

Sohrmann, M., S. Schmidt, I. Hagan, and V. Simanis. 1998. Asymmetric segregation on spindle poles of the *Schizosaccharomyces pombe* septum-inducing protein kinase Cdc7p. *Genes Dev*. 12:84–94.

Tatebe, H., G. Goshima, K. Takeda, T. Nakagawa, K. Kinoshita, and M. Yanagida. 2001. Fission yeast living mitosis visualized by GFP-tagged gene products. *Micron*. 32:67–74.

R Core Team. R: A language and environment for statistical computing. 2018. R Foundation for Statistical Computing.

Tebbs, I.R., and T.D. Pollard. 2013. Separate roles of IQGAP Rng2p in forming and constricting the *Schizosaccharomyces pombe* cytokinetic contractile ring. *Mol Biol Cell*. 24:1904–1917.

Thévenaz, P., U.E. Ruttimann, and M. Unser. 1998. A pyramid approach to subpixel registration based on intensity. *IEEE Trans Image Process*. 7:27–41.

Thiyagarajan, S., E.L. Munteanu, R. Arasada, T.D. Pollard, and B. O'Shaughnessy. 2015. The fission yeast cytokinetic contractile ring regulates septum shape and closure. *J Cell Sci*. 128:3672–3681.

van Unen, J., N.R. Reinhard, T. Yin, Y.I. Wu, M. Postma, T.W.J. Gadella, and J. Goedhart. 2015. Plasma membrane restricted RhoGEF activity is sufficient for RhoA-mediated actin polymerization. *Sci. Rep.* 5:14693.

Vavylonis, D., J.-Q. Wu, S. Hao, B. O'Shaughnessy, and T.D. Pollard. 2008. Assembly mechanism of the contractile ring for cytokinesis by fission yeast. *Science*. 319:97–100.

Venkatram, S., J.L. Jennings, A. Link, and K.L. Gould. 2005. Mto2p, a novel fission yeast protein required for cytoplasmic microtubule organization and anchoring of the cytokinetic actin ring. *Mol Biol Cell*. 16:3052–3063.

Wachtler, V., Y. Huang, J. Karagiannis, and M.K. Balasubramanian. 2006. Cell cycle-dependent roles for the FCH-domain protein Cdc15p in formation of the actomyosin ring in *Schizosaccharomyces pombe*. *Mol Biol Cell*. 17:3254–3266.

Walker, B.J., T. Abeel, T. Shea, M. Priest, A. Abouelliel, S. Sakthikumar, C.A. Cuomo, Q. Zeng, J. Wortman, S.K. Young, and A.M. Earl. 2014. Pilon: an integrated tool for comprehensive microbial variant detection and genome assembly improvement. *PLoS ONE*. 9:e112963.

Wang, N., L. Lo Presti, Y.-H. Zhu, M. Kang, Z. Wu, S.G. Martin, and J.-Q. Wu. 2014. The novel proteins Rng8 and Rng9 regulate the myosin-V Myo51 during fission yeast cytokinesis. *J Cell Biol*. 205:357–375.

Wickham, H. 2017. tidyverse: Easily Install and Load the “Tidyverse.”

Wood, V., R. Gwilliam, M.-A. Rajandream, M. Lyne, R. Lyne, A. Stewart, J. Sgouros, N. Peat, J. Hayles, S. Baker, D. Basham, S. Bowman, K. Brooks, D. Brown, S. Brown, T. Chillingworth, C. Churcher, M. Collins, R. Connor, A. Cronin, P. Davis, T. Feltwell, A. Fraser, S. Gentles, A. Goble, N. Hamlin, D. Harris, J. Hidalgo, G. Hodgson, S. Holroyd, T. Hornsby, S. Howarth, E.J. Huckle, S. Hunt, K. Jagels, K. James, L. Jones, M. Jones, S. Leather, S. McDonald, J. McLean, P. Mooney, S. Moule, K. Mungall, L. Murphy, D. Niblett, C. Odell, K. Oliver, S. O'Neil, D. Pearson, M.A. Quail, E. Rabbinowitsch, K. Rutherford, S. Rutter, D. Saunders, K. Seeger, S. Sharp, J. Skelton, M. Simmonds, R. Squares, S. Squares, K. Stevens, K. Taylor, R.G. Taylor, A. Tivey, S. Walsh, T. Warren, S. Whitehead, J. Woodward, G. Volckaert, R. Aert, J. Robben, B. Grymonprez, I. Weltjens, E. Vanstreels, M. Rieger, M. Schäfer, S. Müller-Auer, C. Gabel, M. Fuchs, A. Düsterhöft, C. Fritzc, E. Holzer, D. Moestl, H. Hilbert, K. Borzym, I. Langer, A. Beck, H. Lehrach, R. Reinhardt, T.M. Pohl, P. Eger, W. Zimmermann, H. Wedler, R. Wambutt, B. Purnelle, A. Goffeau, E. Cadieu, et al. 2002. The genome sequence of *Schizosaccharomyces pombe*. *Nature*. 415:871–880.

Wu, J.-Q., J.R. Kuhn, D.R. Kovar, and T.D. Pollard. 2003. Spatial and temporal pathway for assembly and constriction of the contractile ring in fission yeast cytokinesis. *Dev Cell*. 5:723–734.

Yamashita, A., M. Sato, A. Fujita, M. Yamamoto, and T. Toda. 2005. The roles of fission yeast ase1 in mitotic cell division, meiotic nuclear oscillation, and cytokinesis checkpoint signaling. *Mol Biol Cell*. 16:1378–1395.

Zhang, Q., M.K. Magnusson, and D.F. Mosher. 1997. Lysophosphatidic acid and microtubule-destabilizing agents stimulate fibronectin matrix assembly through Rho-dependent actin stress fiber formation and cell contraction. *Mol Biol Cell*. 8:1415–1425.

Zhang, W., Y. Yu, F. Hertwig, J. Thierry-Mieg, W. Zhang, D. Thierry-Mieg, J. Wang, C. Furlanello, V. Devanarayan, J. Cheng, Y. Deng, B. Hero, H. Hong, M. Jia, L. Li, S.M. Lin, Y. Nikolsky, A. Oberthuer, T. Qing, Z. Su, R. Volland, C. Wang, M.D. Wang, J. Ai, D. Albanese, S. Asgharzadeh, S. Avigad, W. Bao, M. Bessarabova, M.H. Brilliant, B. Brors, M. Chierici, T.-M. Chu, J. Zhang, R.G. Grundy, M.M. He, S. Hebbring, H.L. Kaufman, S. Lababidi, L.J. Lancashire, Y. Li, X.X. Lu, H. Luo, X. Ma, B. Ning, R. Noguera, M. Peifer, J.H. Phan, F. Roels, C. Rosswog, S. Shao, J. Shen, J. Theissen, G.P. Tonini, J. Vandesompele, P.-Y. Wu, W. Xiao, J. Xu, W. Xu, J. Xuan, Y. Yang, Z. Ye, Z. Dong, K.K. Zhang, Y. Yin, C. Zhao, Y. Zheng, R.D. Wolfinger, T. Shi, L.H. Malkas, F. Berthold, J. Wang, W. Tong, L. Shi, Z. Peng, and M. Fischer. 2015. Comparison of RNA-seq and microarray-based models for clinical endpoint prediction. *Genome Biol.* 16:133.

Zhou, Z., E.L. Munteanu, J. He, T. Ursell, M. Bathe, K.C. Huang, and F. Chang. 2015. The contractile ring coordinates curvature-dependent septum assembly during fission yeast cytokinesis. *Mol Biol Cell*. 26:78–90.

Zimmerman, S., and F. Chang. 2005. Effects of γ-tubulin complex proteins on microtubule nucleation and catastrophe in fission yeast. *Mol Biol Cell*. 16:2719–2733.

Zimmerman, S., R.R. Daga, and F. Chang. 2004. Intra-nuclear microtubules and a mitotic spindle orientation checkpoint. *Nat Cell Biol*. 6:1245–1246.

Figures

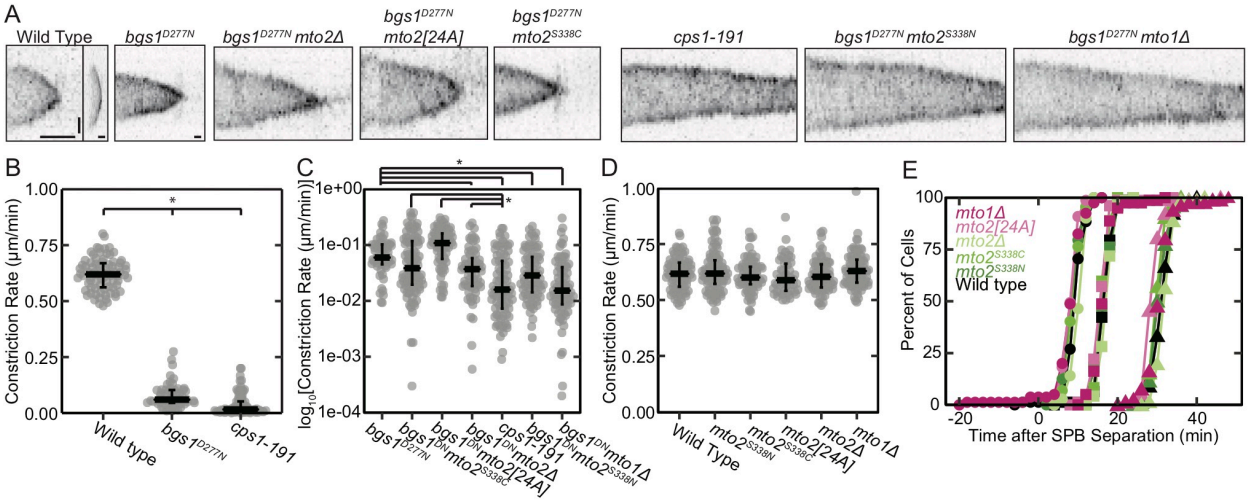

Figure 1. Both the *bgs1^{D277N}* and the *mto2^{S338N}* mutations are required to cause the *cps1-191* constriction phenotype in a wild-type background. A) Kymographs of inverted contrast, maximum-intensity projected images of contractile rings in strains with Rlc1-tdTomato at 36°C. Wild-type cells were imaged at 1-min intervals, and *bgs1^{D277N}* and *cps1-191* cells were imaged with 5-min intervals. The kymograph of the wild-type cell is displayed (left sub-panel) as acquired and (right sub-panel) rescaled to match the timescale of the kymographs (other panels) of the *cps1-191* and six different *bgs1^{D277N}* strains. Horizontal scale bars = 15 min, vertical scale bar = 1 µm. B) Rates of cytokinetic ring constriction measured from a subset of kymographs in A. The data are not normally distributed, so the median and 1st and 3rd quartiles are indicated by black bars, n ≥ 55 cells. C) Log_{10}-transformed cytokinetic ring constriction rates of cells carrying the *bgs1^{D277N}* mutation measured from kymographs as in A. The median and 1st and 3rd quartiles are indicated by black bars, n ≥ 57 cells. Significance differences were determined by Welch's ANOVA followed by Tukey post-hoc test ($p < 0.05$). D) Cytokinetic ring constriction rates of cells carrying *bgs1^{+}* measured from kymographs as in A. The median and 1st and 3rd quartiles are indicated by black bars. No significant differences were detected by Welch's ANOVA. E) Cumulative distribution plots showing accumulation of cells with rings that have (●) assembled, (■) initiated constriction, and (▲) completed constriction in wild-type and *bgs1^{+}* cells with various additional mutations at 36°C. n ≥ 71 cells for C and D.

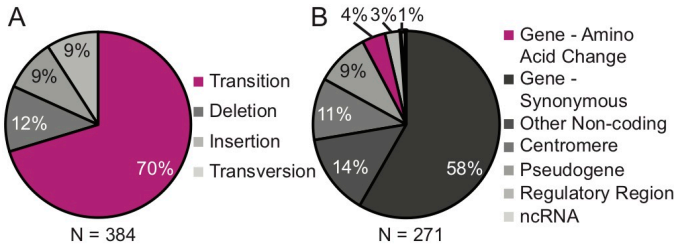

Figure 2. The *cps1-191* strain carries many mutations. A) Categorization of mutation types in *cps1-191*. B) Locations of *cps1-191* transition mutations.

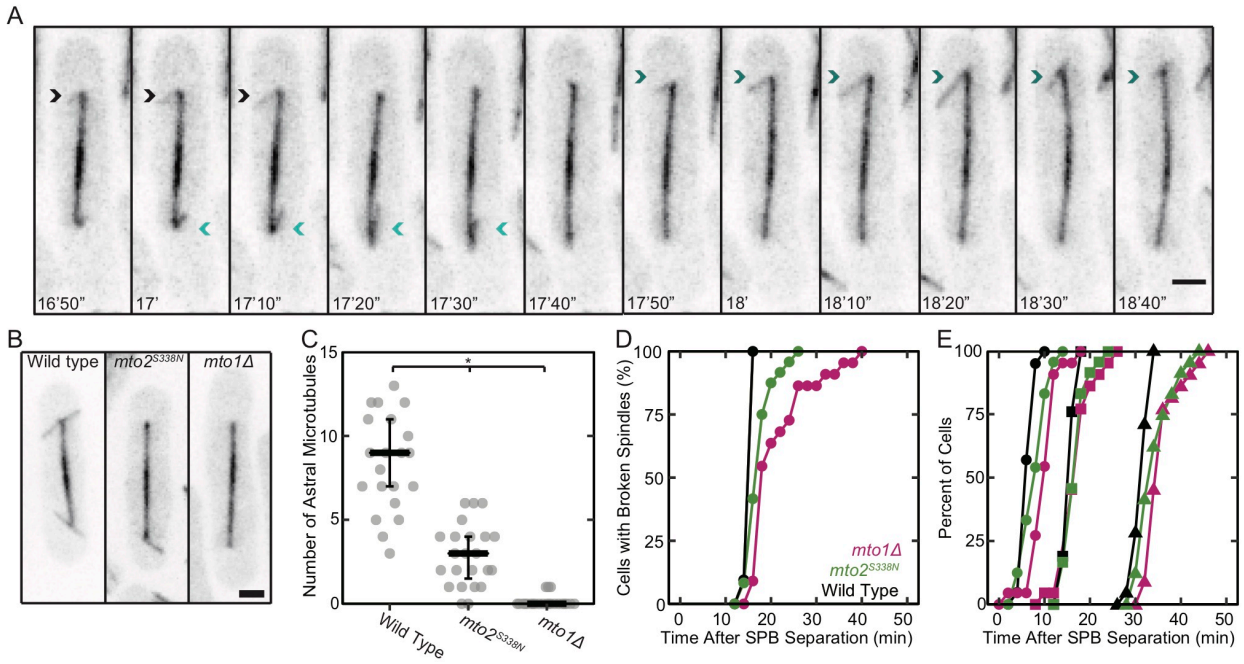

Figure 3. The *mto2*^{S338N} and *mto1Δ* mutations perturb astral microtubules and the time of spindle breakage. A) Time series of inverted contrast maximum-intensity projected fluorescence micrographs of wild type cells at 36°C with astral microtubules labeled with GFP-Atb2 (α tubulin). Arrows of the same color mark the same astral microtubule in consecutive frames. Scale bar 2 µm. B) Representative fluorescence micrographs of three strains (wild type, *mto2*^{S338N}, and *mto1Δ*) at 36°C with spindle microtubules labeled with GFP-Atb2. Scale bar 2 µm. C) The number of astral microtubules nucleated from a single SPB over the course of mitosis at 36°C in wild-type, *mto2*^{S338N}, and *mto1Δ* cells, n ≥ 21 spindle poles. Significance was determined using pairwise K-S tests with Bonferroni correction. D & E) Cumulative distribution plots comparing mitotic and cytokinetic outcomes in wild type, *mto2*^{S338N}, and *mto1Δ* cells with GFP-Atb2 to mark microtubules, Rlc1-tdTomato to mark the cytokinetic ring, and Sfi1-mCherry to mark SPBs at 36°C, n ≥ 21 cells. D) Time course after time zero of the accumulation of cells with broken mitotic spindles. E) Time course after time zero of the accumulation of cells with rings that have (●) assembled, (■) initiated constriction, and (▲) completed constriction.

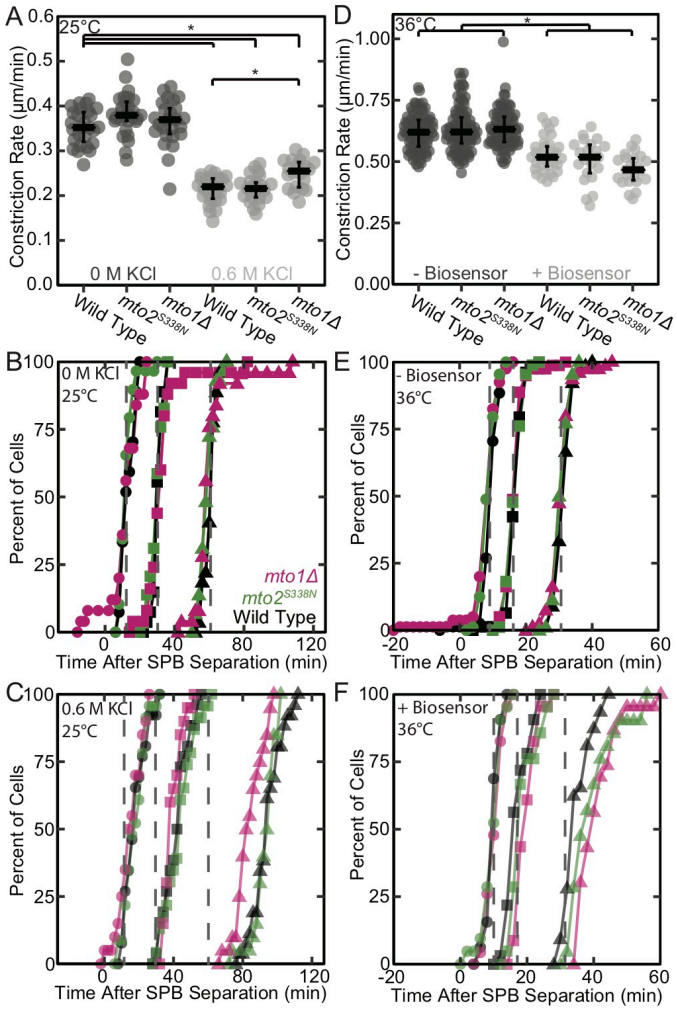

Figure 4. The *mto2*^{S338N} and *mto1Δ* mutations sensitize cells to stresses. A-C) Effects of 0.6 M KCl on cytokinesis in wild type, *mto2*^{S338N}, and *mto1Δ* cells at 25°C. A) Rates of cytokinetic ring constriction. The median and 1st and 3rd quartiles are indicated by black bars and significance ($p < 0.05$) was determined using Welch's ANOVA followed by Tukey post-hoc test. B & C) Time courses of cytokinetic events in cells expressing Rlc1-tdTomato to mark the cytokinetic ring and Pcp1-mEGFP to mark SPBs. Cumulative distribution plots show the accumulation of cells with rings that have (●) assembled, (■) initiated constriction, and (▲) completed constriction in medium with (B) no added KCl or (C) 0.6 M KCl. Dashed gray lines in (B) and (C) indicate the time when 50% of cells in the (B) reach each milestone to facilitate comparison. n ≥ 20 cells for A-C. D-F) Effects of the Rho-GTP biosensor Pkc1(HR1-C2) on cytokinesis at 36°C. D) Rates of cytokinetic ring constriction. The median and 1st and 3rd

quartiles are indicated by black bars and significance ($p < 0.05$) was determined using Welch's ANOVA followed by Tukey post-hoc test. E & F) Cumulative distribution plots comparing mitotic and cytokinetic outcomes in cells (E) without and (F) with the Pkc1(HR1-C2) Rho1 biosensor. Plots show the accumulation of cells with rings that have with (●) assembled , (■) initiated constriction, and (▲) completed constriction. Dashed gray lines in (E) and (F) indicate the time when 50% of cells in the (F) reach each milestone to facilitate comparison. $n \geq 21$ cells for D-F.

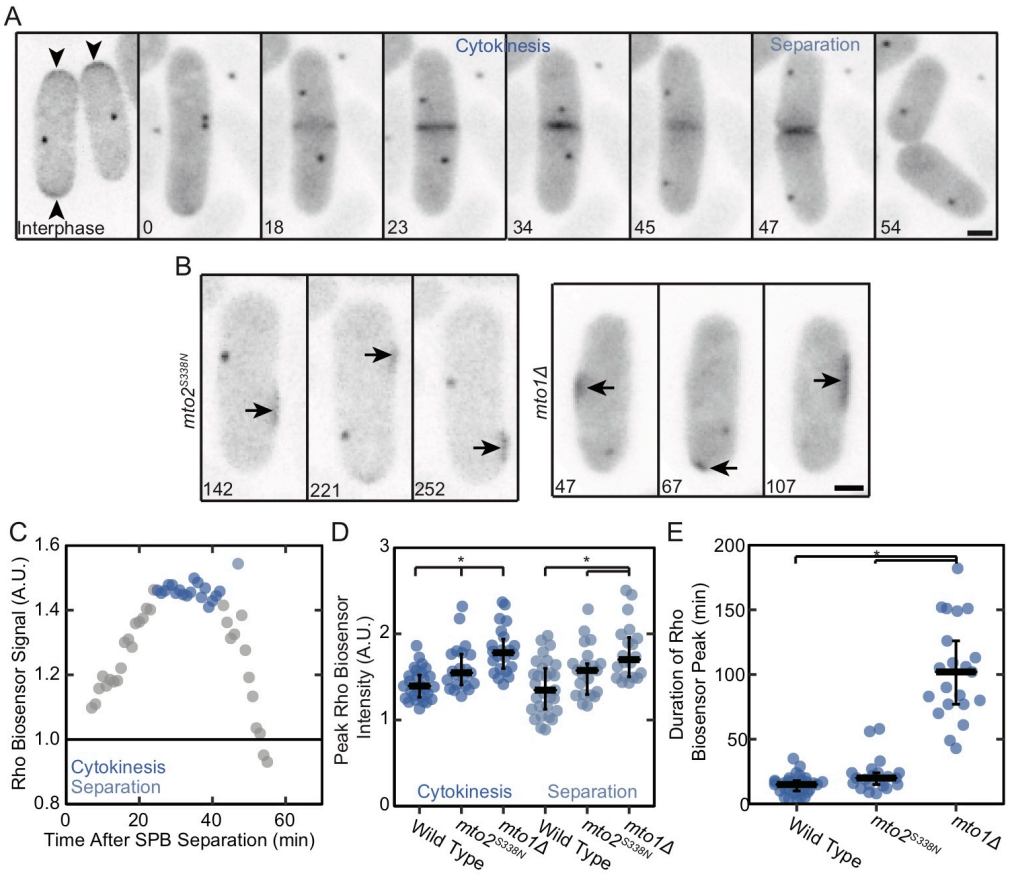

Figure 5. The *mto2*^{S338N} and *mto1Δ* mutations disrupt Rho signaling. A & B) Time series (min) at 36°C of inverted contrast maximum-intensity projected fluorescence micrographs of a wild-type cell expressing the Rho biosensor Pkc1(HR1-C2)-mEGFP and Pcp1-mEGFP to mark spindle pole bodies. Scale bars 2 µm. A) Wild-type cells. Active Rho concentrates at poles of interphase cells (arrowheads) and at the equator of cells during cytokinesis and septation. Times are minutes after SPB separation. B) Representative images of *mto1Δ* and *mto2*^{S338N} cells during interphase showing fluctuating, ectopic concentrations of the biosensor (arrows) at times denoted in minutes after the start of image acquisition. Ectopic accumulations were observed in 23% of wild-type, 49% of *mto2*^{S338N}, and 46% of *mto1Δ* cells; $n \geq 72$ cells, $p < 0.05$ by Chi-Squared test with Bonferroni correction for multiple comparisons. C) Time course of the integrated density of the Rho biosensor at equator of the cell in (A) during cytokinesis normalized to interphase value. The main peak (dark blue) is during furrow formation and the short second peak (light blue) is at cell separation. D & E) Rho biosensor signals at the equators of populations of ≥ 21 cells. Significance ($p < 0.05$) was determined using Welch's ANOVA and Tukey's post-hoc analysis.

D) Peak Rho biosensor signal at the equator during cytokinesis and separation. E) Duration of Rho biosensor peak during cytokinesis.

Table 1. Mutations in ORFs in the *cps1-191* strain.

Gene	Description	Mutation(s)	Chromosome	Location
tlh1	RecQ type DNA helicase	A1570T	I	5662
nup40	Nucleoporin	T281I	I	1353659
mto2	γ-tubulin complex linker	S338N	II	494742
cct1	Chaperonin-containing T-complex α-subunit	R269N	II	2307436
SPBC19G7.04	HMG box protein (predicted)	A211V	II	2349593
bgs1	Linear 1,3-β-glucan synthase catalytic subunit	D277N	II	2356243
mae2	Malic enzyme/malate dehydrogenase	D328G, G332D, N131S	III	277211
ers1	RNA-silencing factor	I209L	III	801197